

# Flow Patterns, Roller Characteristics, and Air Entrainment in Weak Hydraulic Jumps: Does Size Matter?

**Jorge Estrella**

School of Civil Engineering,  
The University of Queensland,  
Brisbane QLD 4072, Australia

**Davide Wüthrich**<sup>1</sup>

School of Civil Engineering,  
The University of Queensland,  
Brisbane QLD 4072, Australia

**Hubert Chanson**

Professor  
School of Civil Engineering,  
The University of Queensland,  
Brisbane QLD 4072, Australia

*A hydraulic jump is a stationary transition from an upstream supercritical to a downstream subcritical flow. Hydraulic jumps with relatively low Froude numbers may be observed downstream of low-head hydraulic structures and their flow properties have not been well documented. In this study, the hydraulic properties were investigated experimentally in weak hydraulic jumps with an inflow Froude number  $Fr_1 = 2.1$  and inflow depths  $0.012\text{ m} < d_1 < 0.130\text{ m}$ . Three novel features of the study were (1) the very wide range of inflow length scales tested systematically, (2) the relatively high Reynolds number  $Re = 3.05 \times 10^5$  achieved in the largest experiment, with the Reynolds number defined as  $Re = \rho \times V_1 \times d_1 / \mu$ , and (3) the broad range of inflow conditions. Although no air entrainment was observed at the lowest Reynolds numbers, some distinct air–water flow patterns were observed in the roller region, generally similar to those observed at higher Froude numbers. The ratio of downstream to upstream depths followed closely the analytical solution of the momentum principle irrespective of the inflow depth. On the other hand, noticeable scaling issues were observed in terms of the dimensionless roller length, length of air–water flow region, roller toe fluctuation frequency, and rate of air entrainment, with increasing dimensionless data with increasing inflow depths, hence Reynolds numbers. The present results have some practical implication in terms of physical modeling and upscaling of results for low-head hydraulic structures, including culverts and storm waterways, which typically operate with Reynolds numbers in excess of  $10^5$ .*  
[DOI: 10.1115/1.4053581]

*Keywords: weak hydraulic jump, flow patterns, roller properties, physical modeling, scaling, air entrainment, low-head hydraulic structures*

## 1 Introduction

A hydraulic jump is a stationary change from an upstream torrential to a downstream fluvial motion [1,2]. It may commonly be encountered in irrigation canals, storm waterways, low-head hydraulic structures (e.g., culverts, weirs), water treatment plants and chemical processing plants, as well as in natural channels (Fig. 1). Although an open channel transition from fluvial to torrential is a relatively smooth process, e.g., at a weir crest, a hydraulic jump may be characterized by a strong dissipative mechanism [3]. While some hydraulic jumps appear like smooth undular waves with almost negligible free-surface turbulence [4], most jumps involve a vigorously tumbling flow region, called the roller. Experimental observations indicated several types of hydraulic jumps, depending upon the upstream Froude number [5,6]. In rectangular horizontal channels, the main types include undular jump, weak jump, oscillating jump, steady jump, and strong jump with increasing Froude numbers [7] (p. 395), although this classification must be considered as a very rough guideline.

Considering a hydraulic jump in a smooth horizontal rectangular channel, the application of the equations of conservation of mass and momentum in an integral form gives two relationships between the conjugate flow properties, i.e., the properties of upstream and downstream of the jump [6,8]

$$\frac{d_2}{d_1} = \frac{1}{2} \times \left( \sqrt{1 + 8 \times Fr_1^2} - 1 \right) \quad (1)$$

$$\frac{Fr_2}{Fr_1} = \frac{2^{3/2}}{\left( \sqrt{1 + 8 \times Fr_1^2} - 1 \right)^{3/2}} \quad (2)$$

where  $d$  is the water depth,  $Fr$  is the Froude number  $Fr = V / (g \times d)^{1/2}$ ,  $g$  is the gravity constant,  $V$  is the flow velocity, and the subscripts 1 and 2 are the upstream and downstream flow properties, respectively.

Because of their design implications, the vast majority of previous hydraulic jump studies were conducted with relatively large inflow Froude numbers ( $Fr_1 > 3$ ), with a few exceptions detailed in Table 1. A few studies investigated the turbulence in the water phase [9,10,13], while the air–water flow properties were studied for a few limited conditions [11,12,14]. All these research studies were undertaken for relatively low Reynolds numbers, with the Reynolds number defined as  $Re = \rho \times V_1 \times d_1 / \mu$ . Further, none tested the potential scale effects when extrapolating the results to full-scale low-head hydraulic structures (Fig. 1) and in several environmental phenomena related to water management and water quality.

To date, the characteristics of weak hydraulic jumps remain largely unexplored. This study aims to provide a more detailed characterization of breaking jumps with small Froude number ( $Fr_1 = 2.1$ ), across a relatively large range of inflow depths, i.e.,  $0.012\text{ m} < d_1 < 0.130\text{ m}$ . More specifically, a range of hydraulic parameters were compared systematically, encompassing flow patterns (Sec. 3), roller's free-surface characteristics (Sec. 4) and

<sup>1</sup>Current address: Department of Hydraulic Engineering, Delft University of Technology, Delft 2600, The Netherlands.

Contributed by the Fluids Engineering Division of ASME for publication in the JOURNAL OF FLUIDS ENGINEERING. Manuscript received September 22, 2021; final manuscript received January 10, 2022; published online February 23, 2022. Assoc. Editor: Ning Zhang.



(a)



(b)

**Fig. 1** Photographs of weak hydraulic jumps in man-made channels: (a) hydraulic jump in a culvert outlet in Brisbane (Australia) on February 6, 2020 and (b) hydraulic jump downstream of the “sticky rice” bridge, Puli (Taiwan) on April 13, 2019

air entrainment (Secs. 5 and 6). The largest experimental configuration corresponded to a unit discharge comparable to, or larger than, that of the prototype hydraulic jumps seen in Figs. 1(a) and 1(b), thus allowing a relevant discussion in terms of scale effects and upscaling issues related to environmental flows (Sec. 7).

## 2 Experimental Facilities, Instrumentation, and Methodology

A physical modeling approach is used herein, as it is expected to deliver a reliable prediction of the performances of a prototype structure [16]. However, this modeling approach must rely upon the fundamental principles of similitude, and the present investigation was based upon a Froude similitude using the same fluids, water and air, in all the experiments. This leads to an underestimation of the Reynolds number and therefore of its turbulent properties. For this reason, different values of  $Re$  were systematically tested to ensure reliability of these results and detect any scale effect. All tests were performed in three different rectangular flumes at the University of Queensland (Australia) (Table 1). For channel 1, the internal width was  $B = 0.50$  m, the test section length was 3.2 m, and the horizontal invert was made of high density poly ethylene (HDPE), while the sidewalls were 0.40 m high made of glass to ensure maximum visibility. The inflow conditions were controlled by a vertical gate equipped with a semicircular shape ( $\varnothing = 0.3$  m), and the tailwater conditions were set by a vertical overshoot gate located at the downstream end of the test

section. Channel 2 was a 12 m long 0.5 m wide tilting flume, with a slope set at  $S_o = 0.016$ . The bed was made of polyvinyl chloride (PVC) and the sidewalls were in glass. The inflow was uncontrolled and the tailwater conditions were controlled by a radial gate. Channel 3 was 19 m long, 0.7 m wide and the bed slope was fixed:  $S_o = 0.0132$ . The bed was made of PVC and the sidewalls were in glass. As for channel 2, the inflow was uncontrolled and the tailwater conditions were controlled by a radial gate in channel 3.

The water was delivered by a constant head reticulation system in channels 1 and 2, enabling a very stable discharge into the upstream head tank controlled by the upstream vertical sluice. Channel 3 was fed by two pumps regulated by an electronic controller. The water discharge was measured with a Venturi meter, an orifice meter, and a magnetoflowmeter in channels 1, 2, and 3, respectively, designed based upon British Standard [17]. The clear-water flow depths were measured using rail mounted point gages with a 0.5 mm accuracy. In channel 1, the void fraction data were recorded with a needle probe ( $\varnothing = 0.25$  mm). The needle probe design is an intrusive phase-detection sensor designed to pierce the bubbles [18], and its operation is based upon the difference in electrical conductivity between water and air [19]. The needle probe signal output was recorded at 20 kHz for 45 s and processed using a single threshold technique set at 50% of the air and water voltages [20]. The movement of the probe in the vertical direction was controlled by a fine adjustment system connected to a HAFCO™ digital scale unit with a vertical accuracy of less than 0.1 mm. The measurements were conducted on the channel centerline and the longitudinal position accuracy was within  $\pm 5$  mm. The experiments were visually documented with a DSLR camera Pentax™ K-3 and a digital camera Casio™ Exilim EX-10.

The basic flow pattern observations and free-surface recordings were conducted in hydraulic jumps with inflow Froude number  $Fr_1 = 1.95$  and 2.1, with inflow depths within  $0.012 \text{ m} < d_1 < 0.130 \text{ m}$ , and for unit discharges within  $0.0078 \text{ m}^2/\text{s} < q < 0.31 \text{ m}^2/\text{s}$  (Table 1). The void fraction measurements were conducted in hydraulic jumps with an inflow Froude number  $Fr_1 = 2.1$ , with inflow depths within  $0.045 \text{ m} < d_1 < 0.130 \text{ m}$ , and for unit discharges within  $0.063 \text{ m}^2/\text{s} < q < 0.31 \text{ m}^2/\text{s}$ . The large majority of channel 1 experiments was undertaken with the jump toe located at a dimensionless longitudinal position  $x_1/d_1 \approx 15$ , except for the largest upstream depth  $d_1 = 0.130$  m for which the jump toe location was  $x_1/d_1 \approx 9$ . These conditions corresponded to partially developed inflow conditions. In channels 2 and 3, the inflows were fully developed corresponding to a gradually varied S2 backwater profile. The present flow conditions are compared to previous experiments in weak hydraulic jumps on smooth rectangular channels in Table 1.

## 3 Visual Observations and Flow Patterns

Despite its weak nature, the visual observations showed a hydraulic jump with a marked roller region for all investigated flow conditions. In all three channels, the roller features however differed substantially between inflow depths (Fig. 2) and the jump roller tended to become visually more turbulent for increasing inflow depths, hence Reynolds number, for a constant inflow Froude number  $Fr_1 = 2.1$  (or 1.95). Typical flow patterns are illustrated in Fig. 2. The upstream flow basically presented a smooth continuous free surface and had some low level of turbulence. Its appearance contrasted drastically with the complicated surface of the breaking roller, forming a key feature of the hydraulic jump. The upstream edge of the hydraulic jump is termed herein as the “roller toe.” For all tested flow conditions, the roller toe perimeter was a well-defined line separating the relatively smooth upstream flow motion and the breaking roller (Fig. 2). The roller toe constantly fluctuated in both longitudinal and transverse directions about its mean position. Downstream of the roller toe, the visual records indicated a strongly turbulent flow, with free-surface

**Table 1** Experimental studies of weak hydraulic jumps in smooth flat rectangular channels ( $Fr_1 < 3$ )

Reference	$S_o$	$B$	$h$	$Q$	$x_j$	$d_1$	$x_j/d_1$	$Fr_1$	Re
This study	0	(m) 0.50	(m) 0.012	(m <sup>3</sup> /s) 0.0039	(m) 0.19	(m) 0.012	15.8	1.9	$7.7 \times 10^3$
			0.024	0.0146	0.38	0.027	14.1	2.1	$2.9 \times 10^4$
			0.045	0.0316	0.71	0.045	15.8	2.1	$6.3 \times 10^4$
			0.070	0.0620	1.11	0.071	15.6	2.1	$1.2 \times 10^5$
			0.095	0.0991	1.50	0.097	15.65	2.1	$2.0 \times 10^5$
	0.016	0.50	0.130	0.1535	1.20	0.130	9.2	2.1	$3.0 \times 10^5$
			N/A	0.0186	7.35	0.0315	233	2.12	$3.7 \times 10^4$
				0.0237	7.5	0.038	197	2.05	$4.7 \times 10^4$
				0.0387	7.4	0.051	145	2.14	$7.7 \times 10^4$
				0.0589	7.25	0.068	106	2.12	$1.2 \times 10^5$
	0.0132	0.70	N/A	0.0461	10.0	0.058	202	1.94	$6.5 \times 10^4$
				0.0584	10.9	0.049	186	1.91	$8.3 \times 10^4$
				0.0996	10.5	0.082	127	1.94	$1.4 \times 10^5$
				0.0077	—	0.0197	—	2.99	$2.5 \times 10^4$
				0.02178	<0.02	0.0862	<0.2	1.2	$7.2 \times 10^4$
Lennon and Hill [9]	—	0.30	—	0.0077	—	0.0197	—	2.99	$2.5 \times 10^4$
Misra et al. [10]	—	0.30	—	0.02178	<0.02	0.0862	<0.2	1.2	$7.2 \times 10^4$
Murzyn et al. [11]	0	0.30	0.09	0.0265	0.43	0.059	7.3	2.0	$8.8 \times 10^4$
			0.07	0.0226	0.44	0.046	9.6	2.4	$7.5 \times 10^4$
			0.04	0.0099	0.18	0.029	6.2	2.1	$3.3 \times 10^4$
			0.07	0.0170	0.29	0.045	6.4	1.9	$5.6 \times 10^4$
			0.09	0.0266	0.43	0.059	7.3	2.0	$8.8 \times 10^4$
Chachereau and Chanson [12]	0	0.50	0.036	0.033	1.50	0.0420	35.7	2.4	$6.6 \times 10^4$
				0.0365		0.0425	35.3	2.7	$7.2 \times 10^4$
				0.040		0.0438	34.2	2.8	$7.9 \times 10^4$
				0.0446		0.0454	33.0	2.9	$8.9 \times 10^4$
Mignot and Cienfuegos [13]	0	0.95	—	0.164	0.35	0.118	3.0	1.88	$1.7 \times 10^5$
					1.4	0.120	11.7	1.99	
Lin et al. [14]	0	0.50	—	0.0102	0.7	0.0192	36.5	2.43	$3.4 \times 10^4$
Montano and Felder [15]	0.022	0.50	N/A	0.20	—	0.154	—	2.1	$4.0 \times 10^5$

Note:  $B$ : rectangular channel width;  $d_1$ : upstream water depth;  $Fr_1$ : upstream Froude number defined in terms of upstream flow depth;  $h$ : upstream gate opening;  $Q$ : discharge; Re: Reynolds number;  $S_o$ : longitudinal bed slope;  $x_j$ : longitudinal distance from upstream gate; (—): information not available; and N/A: not applicable.

distortion and breaking of the roller, typically associated with surface waves, surface scars, water projections, sometimes with surface breaking and ejection of drops, entrainment of bubbles, including two-phase air–water mixture flow. Scars were observed at the free surface, suggesting the occurrence of upwelling boils and submerged large vortices. In the second half of the roller, these scars interacted further with rising bubbles driven by buoyancy toward the free surface. However, these features revealed some differences linked to the Reynolds number, further detailed hereafter.

At the smallest in-flow depth ( $d_1 = 0.012$  m,  $Re = 7.75 \times 10^3$ ), the hydraulic jump's free surface was dominated by small-scale turbulent features, with free-surface length scales smaller than 0.01 m, for which surface tension was able to maintain some cohesion of the liquid, thus preventing air bubble entrainment (Fig. 2(a)). This type of flow corresponded to a turbulent flow with surface tension dominant and gravity unimportant [21] (region 1). The jump was characterized by a regime of micro-breakers, and the free-surface shape exhibited features similar to that of small kitchen sink jumps [22] and viscous hydraulic jumps [23]. This resulted in the absence of air entrainment visually observed for  $d_1 = 0.012$  m ( $Re = 7.75 \times 10^3$ , Fig. 2(a)).

For  $d_1 > 0.027$  m ( $Re > 2.9 \times 10^4$ ) breaking initiated, generating strong free-surface turbulence [21] (region 2). For these, the free-surface deformations could no longer be restrained by gravity or surface tension and air entrainment occurred because the turbulent Reynolds stresses acting next to the free-surface were large enough to overcome gravity and surface tension [24]. The air entrainment induced a mix of bubbles, drops, foams, packets, with very energetic transient interfacial processes, e.g., breakup, coalescence, rebounds, collapses. In the upper part of the roller, the instantaneous surface separating the water and atmosphere presented a complicated structure, with interpenetrating and interacting gas and liquid phases (e.g., Figs. 2(e) and 2(f)). Physically, the breaking roller presented a number of key features, which were

linked to the inflow conditions and breaking jump turbulence. One visual evidence of strong turbulence was the rapid deformation of the roller free-surface. A number of experimental investigations quantified two-dimensional free-surface fluctuations, showing a high level of turbulence immediately downstream of the impingement perimeter [25–27]. In the current study, the deformation of the roller surface was mostly documented through sidewall photographs and video movies, with the free-surface deformations increasing with increasing Reynolds numbers (e.g., Fig. 2). The strong free-surface turbulence in the breaking process resulted in a number of bubbles entrained within the roller, with a varying length of the air–water region observed through the glass sidewalls. As mentioned, no aeration was observed for  $d_1 = 0.012$  m ( $Re = 7.75 \times 10^3$ , Fig. 2(a)). However, the entrainment of individual bubbles was seen for  $d_1 = 0.027$  m and 0.045 m ( $Re = 2.9 \times 10^4$  and  $6.3 \times 10^4$ ), even if no reliable measurement was possible with the needle probe for  $d_1 = 0.027$  m ( $Re = 2.9 \times 10^4$ ) because of the very small number of entrained bubbles (Sec. 5). Larger amounts of entrained air were observed for  $d_1 > 0.071$  m ( $Re > 1.2 \times 10^5$ ) with two dominant entrainment mechanisms. Namely, (a) air entrapment at the roller toe with some advective convection of air in the mixing layer and (b) interfacial aeration through the roller free-surface in the upstream half of the roller. The former was well-documented in the literature [28–30] while the latter mechanism was first evidenced by Wang and Chanson [31] in hydraulics jumps with larger Froude numbers ( $3.8 < Fr_1 < 10$ ).

#### 4 Free-Surface Characteristics

Free-surface measurements were conducted for all investigated flow conditions (Table 1), focusing on the conjugate depths  $d_2$  and  $d_1$ , the roller length  $L_r$ , the length of the air–water region  $L_{air}$ , and the main oscillation frequency  $F_{toe}$  of the roller toe about its mean position. Herein, the roller length  $L_r$  was defined as the

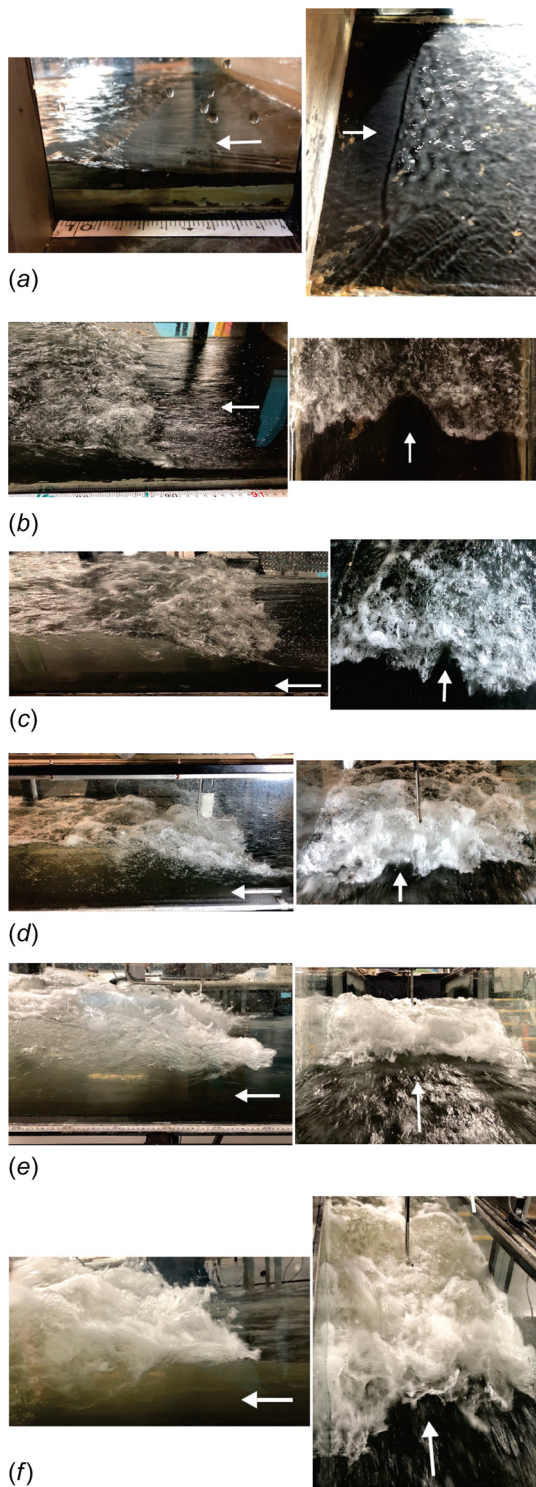


**Fig. 2 Visual observations of hydraulic jump at low Froude number  $Fr_1 = 2.1$  with different inflow depth: side and top views in channel 1—White arrows indicate flow direction: (a)  $d_1 = 0.012$  m,  $Re = 7.75 \times 10^3$ , (b)  $d_1 = 0.027$  m,  $Re = 2.9 \times 10^4$ , (c)  $d_1 = 0.045$  m,  $Re = 6.3 \times 10^4$ , (d)  $d_1 = 0.071$  m,  $Re = 1.2 \times 10^5$ , (e)  $d_1 = 0.097$  m,  $Re = 2.0 \times 10^5$ , and (f)  $d_1 = 0.130$  m,  $Re = 3.05 \times 10^5$ .**

longitudinal distance between the roller toe position  $x_1$  and the location where the water surface became quasi-horizontal, and the downstream depth was measured. The present data are based upon visual observations, and it is acknowledged that the visual observations might slightly underestimate the whole roller length. The

length  $L_{air}$  of the air–water flow region was determined through some sidewall observation of the entrained air bubbles: that is,  $L_{air}$  was the time-averaged length of the bubbly flow region. The oscillation frequency  $F_{toe}$  of the roller toe was deduced from visual observations and corresponded to the dominant frequency of the longitudinal fluctuations.

Upstream of the roller toe, all observations indicated that the free surface was quasi-horizontal. The toe of the jump was characterized by a marked discontinuity in longitudinal free-surface slope  $\partial d/\partial x$ , with a sharp rise in water surface elevation in the downstream direction above the hydraulic jump roller (Fig. 2). The ratio of conjugate depths  $d_2/d_1$  showed some agreement with the momentum equation (Eq. (1)) and the present data are compared to Eq. (1) and previous experimental data in Fig. 3. The dimensionless roller length  $L_r/d_1$  was observed to increase with increasing inflow Froude number [1,11,32]. The present data are compared to previous observations in stationary hydraulic jumps and breaking bores in Fig. 4(a). The data are further compared to the linear trend in Eq. (3) proposed by Wang and Chanson [33]

$$\frac{L_r}{d_1} = 6 \times (Fr_1 - 1) \quad (3)$$

obtained for  $2 < Fr_1 < 10$ . While the present visual observations were qualitatively in agreement with past studies (Fig. 4(a)), the data showed an impact of the inflow depth and Reynolds number  $Re$  on the dimensionless roller length  $L_r/d_c$  (Fig. 4(b)). In Fig. 4(b), the roller length is normalized in terms of the critical flow depth  $d_c$ , and the current dataset is compared to Eq. (3), which is independent of Reynolds number, and to two previous studies undertaken with  $Fr_1 \approx 2$  [11] and  $Fr_1 = 5.1$  [34]. Importantly, all data sets for  $Fr_1 \approx 1.95$  to 2.1 exhibited a marked increase in dimensionless roller length  $L_r/d_c$  with increasing Reynolds number (Fig. 4(b)). Combining all the present data with the observations of Murzyn et al. [11], the dimensionless roller length  $L_r/d_c$  was correlated to the Reynolds number as

$$\frac{L_r}{d_c} = 0.322 \times ((Fr_1 - 1) \times Re)^{0.22} \text{ for } Fr_1 = 1.95 \text{ to } 2.1 \quad (4)$$

with a correlation coefficient of 0.730.

Previous observations showed further an increasing air–water flow region with increasing Froude number. Figure 5 presents the dimensionless length  $L_{air}$  of the air–water flow region as a function of the inflow Froude number (Fig. 5(a)) and Reynolds number (Fig. 5(b)). The current data indicated a marked effect of the inflow depth and Reynolds number on the bubbly flow region extent, for a constant Froude number (Fig. 5(b)). This impact was more dramatic than that for the dimensionless roller length. Noteworthy, the ratio  $L_{air}/L_r$  ranged from 0 to 1.7, with increasing Reynolds number for  $Fr_1 = 2.1$ . The present data were best correlated by

$$\frac{L_{air}}{d_c} = 8.61 \times 10^{-4} \times (Re - 7.75 \times 10^3)^{0.787} \text{ for } Fr_1 = 1.95 \text{ and } 2.1 \quad (5)$$

with a correlation coefficient of 0.878. Equation (5) is compared to the experimental data in Fig. 5(b).

For all investigated flow conditions, the hydraulic jump roller toe shifted longitudinally about its mean position  $x = x_1$ . For  $d_1 = 0.012$  m ( $Re = 7.75 \times 10^3$ ), the fluctuations were relatively slow and barely measurable. For  $d_1 > 0.027$  m ( $Re > 2.9 \times 10^4$ ), the roller toe fluctuated in both fast and slow manners. Herein, the focus was on the fast fluctuations of the mean roller toe position. Such fast fluctuations in roller toe position were recorded in earlier studies [37]. These fluctuations are believed to be linked to the combined effect of the air entrapment at the impingement

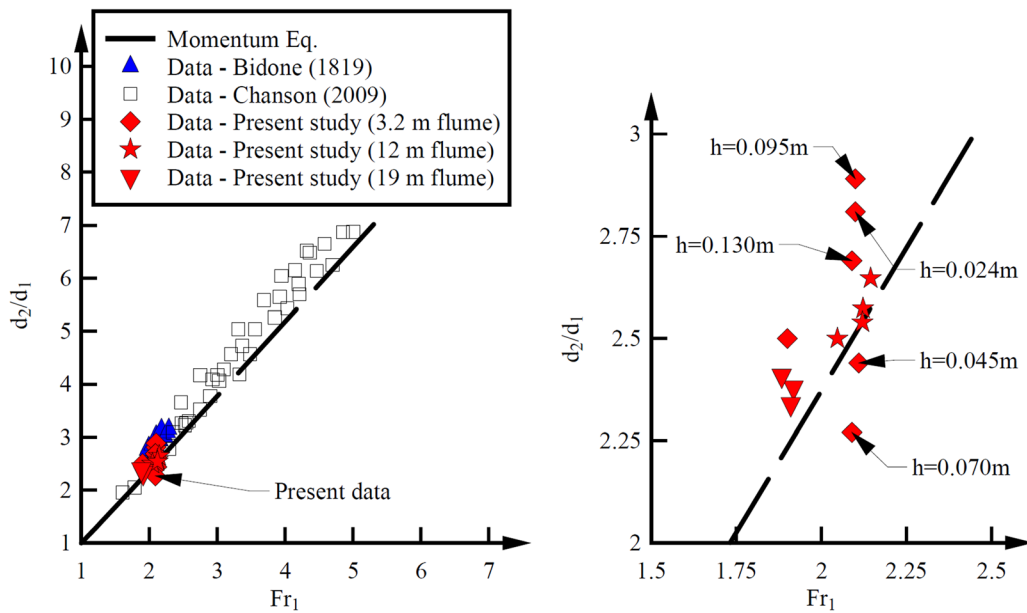


**Fig. 3** Ratio of conjugate depths  $d_2/d_1$  for weak hydraulic jump at low Froude number  $Fr_1 = 1.95$  and  $2.1$  in smooth rectangular channels—comparison with the momentum equation (Eq. (1)) and experimental data [2,32]—inset (right): details of present data with same legend as main figure

point, generation of large Kelvin–Helmholtz vortical structures, their detachment and their advection in the developing shear layer including vortex pairing.

The visual observations of roller toe oscillations showed a dominant frequency  $F_{toe}$ , with results reported in Figs. 6(a) and 6(b) as functions of the inflow Froude number  $Fr_1$  and Reynolds number  $Re$ , respectively. In Fig. 6, the present data are compared to previous observations in hydraulic jumps. Noteworthy, the present observations (Fig. 6(a)) were comparable to Kelvin–Helmholtz (K–H) instability data about  $F_{toe} \times d_1/V_1 \approx 0.07$  [40,41]. Figure 6(a) tends to suggest a decreasing Strouhal number  $F_{toe} \times d_1/V_1$  with increasing Froude number, toward an asymptotic value about 0.005 for  $Fr_1 > 6$ . But, the present data were obtained with a constant Froude number for different Reynolds numbers, and showed higher fluctuation frequencies of the roller toe at larger Reynolds numbers (Fig. 6(b)), whereas no apparent effect of Reynolds number was seen in earlier data sets at higher Froude numbers. It is suggested that the different behavior might reflect a more intense competition between Froude and Reynolds similarity in hydraulic jumps at low Froude numbers, resulting in a more relevant role of viscous forces in weak hydraulic jumps. Namely, the advection of vorticity and of air bubbles was the dominant mechanism affecting the fast fluctuations in roller toe position. The present data showed a monotonic increase in Strouhal number  $F_{toe} \times d_c/V_c$  with increasing Reynolds number best correlated by

$$\frac{F_{toe} \times d_c}{V_c} = 9.23 \times 10^{-7} \times Re + 0.0465 \quad \text{for } Fr_1 = 1.95 \text{ and } 2.1 \quad (6)$$

with a correlation coefficient of 0.956. Equation (6) is compared to the experimental data in Fig. 6(b). Interestingly, recent K–H instability frequency data suggested a similar monotonic trend in terms of the Reynolds number in the form:  $St \propto Re^{1/2}$  [40].

## 5 Air Concentration in the Roller

Hydraulic jumps with a breaking roller may be characterized by substantial air bubble entrainment, yielding some complicated air–water flow motion. Seminal experiments started with

Rajaratnam [42], with further research studies by Chanson and Brattberg [43], and Murzyn et al. [44]. Herein, air concentration measurements were performed in hydraulic jumps with an inflow Froude number  $Fr_1 = 2.1$  and inflow depths  $d_1$  between 0.045 m and 0.130 m, corresponding to Reynolds numbers between  $6.3 \times 10^4$  and  $3.05 \times 10^5$  (Table 1). For  $d_1 = 0.012$  m, no air entrainment was observed (Fig. 2(a)). For  $d_1 = 0.027$  m, very slight individual bubble entrainment was observed visually but it was not detectable by the needle probe sensor (Fig. 2(b)). Detailed air–water flow measurements were conducted for  $d_1 > 0.045$  m, corresponding to  $Re > 6.3 \times 10^4$ .

In the roller region of the weak hydraulic jump, some distinct air–water flow patterns were observed, with similar trends to those observed at higher Froude numbers. Namely the air concentration was zero at the invert and reached unity above the roller surface. In the roller, the vertical profile of air concentrations presented a local maximum in the shear zone for  $1.5 < (x-x_1)/d_1 < 3$ , that is  $0.2 < (x-x_1)/L_r < 0.4$ , with  $x$  the longitudinal coordinate. The upper extent of the roller may be characterized by the elevation  $Y_{90}$  where the air concentration equals 0.90. Figure 7 shows typical air concentration distributions and the data are compared to the longitudinal distributions of the characteristic air–water elevation  $Y_{90}$ , with  $y$  the vertical elevation above the invert. While the results were qualitatively close, the present dataset showed a stronger and longer aeration of the roller at the higher Reynolds numbers (e.g., Fig. 7(b)).

The amount of entrained air may be quantitatively described by the depth-averaged air concentration  $C_{mean}$ , defined as

$$C_{mean} = \frac{1}{Y_{90}} \times \int_{y=0}^{Y_{90}} C \times dy \quad (7)$$

The longitudinal variation of the depth-averaged void fraction  $C_{mean}$  is presented on Fig. 8 for all the measurements. The data showed an initial rapid increase in depth-averaged void fraction, with increasing distance from the roller toe, for  $(x-x_1)/d_1 < 1$ . Further downstream, i.e.,  $(x-x_1)/d_1 > 1$ , the results presented a decreasing trend, corresponding to some flow de-aeration induced by buoyancy effects and some upward bubble migration toward

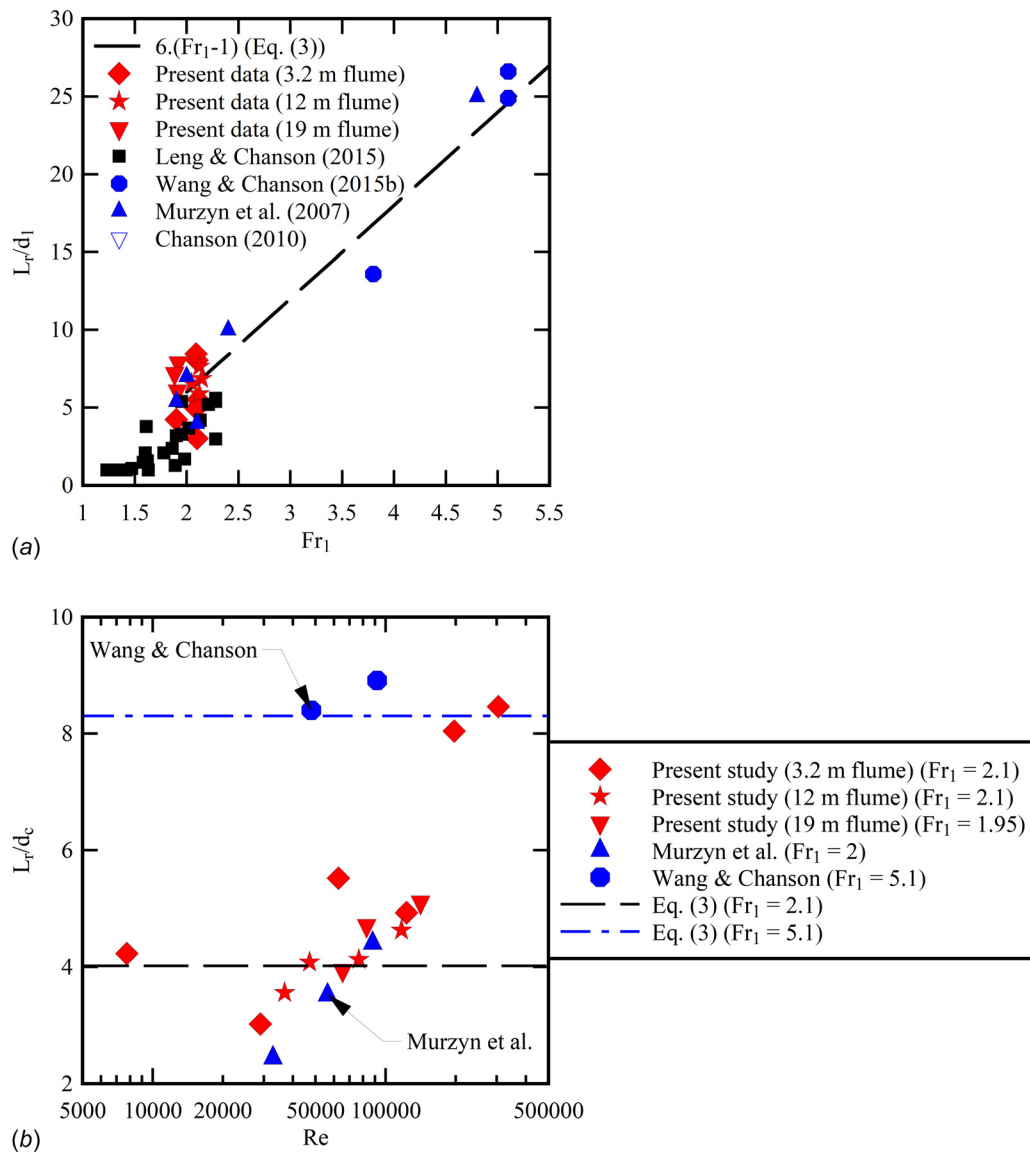


**Fig. 4 Dimensionless roller length for weak hydraulic jump at low Froude number  $Fr_1 = 1.95$  and  $2.1$  in smooth rectangular channels—comparison with Eq. (3) and experimental data in stationary hydraulic jumps [11,34] and breaking bores [35]: (a) dimensionless roller length  $L_r/d_1$  as a function of inflow Froude number  $Fr_1$  and (b) dimensionless roller length  $L_r/d_c$  as a function of Reynolds number  $Re$**

the free surface in the downstream part of the roller. Such a longitudinal trend was consistent with previous studies, typically conducted at higher Froude numbers [12,45].

The longitudinal variations of the characteristic air–water elevations  $Y_{90}$  where  $C = 90$  and equivalent clear water depth  $d$  presented some profiles that were independent on the initial flow depth and therefore of the Reynolds numbers

$$\frac{Y_{90} - d_1}{d_2 - d_1} = \left( \frac{x - x_1}{L_r} \right)^{0.36} \quad (8)$$

$$\frac{d - d_1}{d_2 - d_1} = \left( \frac{x - x_1}{L_r} \right)^{0.69} \quad (9)$$

where the equivalent clear-water depth  $d$  is defined as

$$d = \int_{y=0}^{Y_{90}} (1 - C) \times dy \quad (10)$$

Equations (8) and (9) are compared to the experimental data in Fig. 9. The results were close to monophasic point gauge and ultrasonic sensor data [46] and a theoretical solution [47]. Altogether, the free-surface profiles of the jump roller were similar for all Reynolds numbers.

## 6 Air Entrainment Flux

The air–water flux plays a critical role in a number of environmental processes and the quantification of the dissolved oxygen is an important parameter in the assessment of water quality. The air entrainment flux was computed as

$$q_{\text{air}} = \int_{y=0}^{y=Y_{90}} C \times V_x \times dy \quad (11)$$

where  $C$  is the time-averaged void fraction,  $V_x$  is the interfacial velocity and  $y$  the vertical coordinate, with  $Y_{90}$  the elevation at which  $C = 90\%$ . Weak hydraulic jumps revealed small recirculation zones, implying that their contribution to the total air

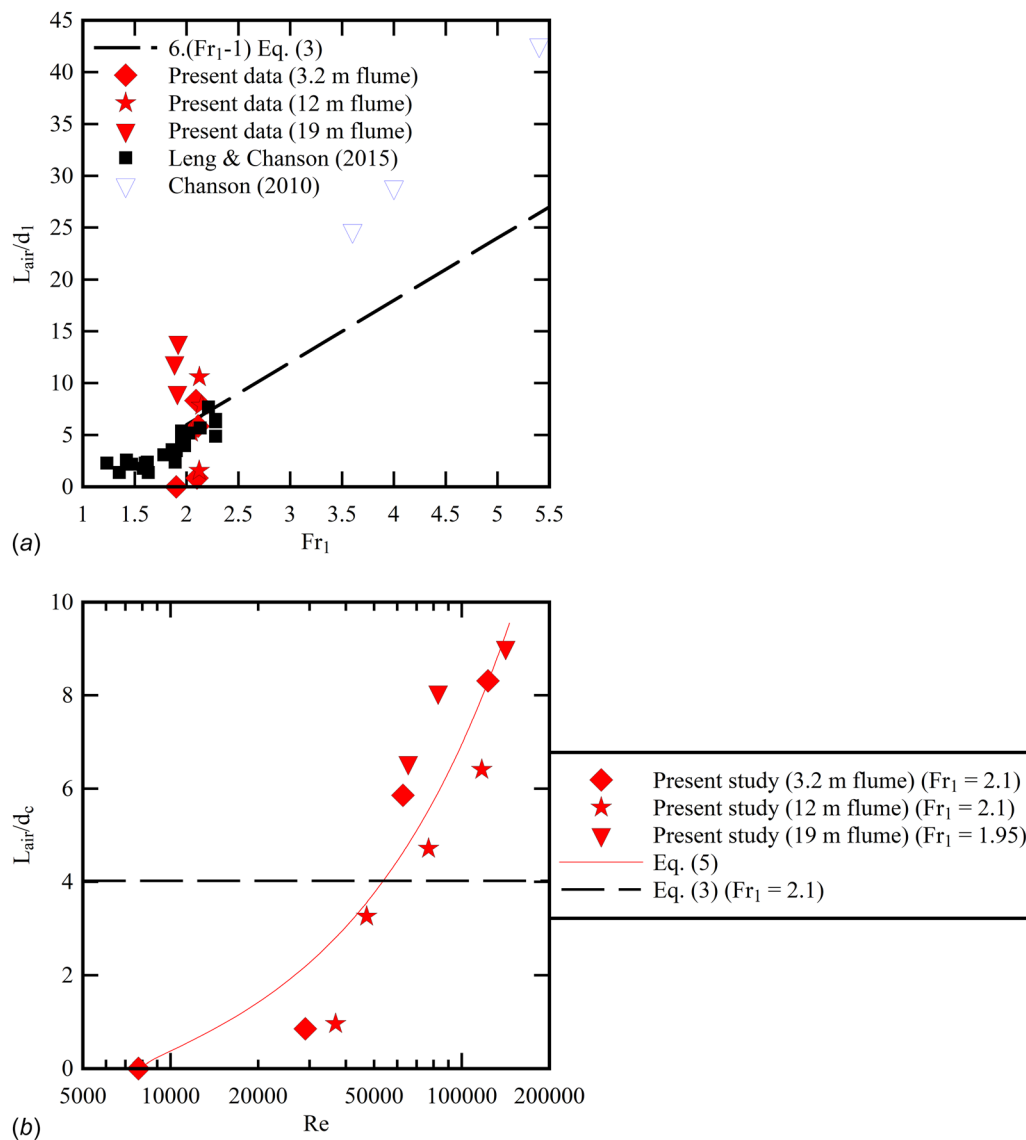


**Fig. 5 Dimensionless air–water flow region length for hydraulic jump at low Froude number  $Fr_1 = 1.95$  and  $2.1$  in smooth rectangular channels—comparison with Eqs. (3) and (5) together with experimental data in stationary hydraulic jumps [36] and breaking bore [35]: (a) dimensionless air–water flow region length  $L_{air}/d_1$  as a function of inflow Froude number  $Fr_1$  and (b) dimensionless air–water flow region length  $L_{air}/d_c$  as a function of Reynolds number  $Re$**

entrainment flux was minimal compared to the shear layer. This is in line with previous data from Wang and Chanson [48], who showed a decreasing behavior for decreasing Froude numbers. For  $Fr_1 = 2.1$ , the ratio of air discharge  $q_{air}$  and water discharge  $q$  is presented in Fig. 10 for four hydraulic jumps with four Reynolds numbers. Results showed almost no air entrainment flux for  $h < 0.045$ , i.e.,  $Re < 6.3 \times 10^4$ , whilst for higher inflow depths and Reynolds numbers, i.e.,  $h > 0.070$  and  $Re > 1.2 \times 10^5$ , the data showed a substantial increase with a peak of  $q_{air}/q \sim 0.3$ – $0.35$  at  $1 < (x-x_1)/d_1 < 1.5$ . This increase in air flux reflected the aeration of the shear layer downstream of the impingement point. The decrease for  $(x-x_1)/d_1 > 1.5$  is associated with the de-aeration process occurring in the downstream part of the roller, where the flow becomes controlled by gravity and buoyancy. Despite the uncertainties linked with the estimation of the air flux, this is consistent with the visual observations in Figs. 2(a) and 2(b) for  $h < 0.045$  and with previous studies by Wang and Chanson [48].

## 7 Discussion on Similarity, Scaling, and Sizes

In hydraulic jumps, the selection of the Froude similitude is based upon some basic theoretical considerations [6,49]. In turn, the Reynolds number differs between different experiments, herein performed with an identical Froude number  $Fr_1 = 2.1$ , because the scaling ratio of the Reynolds number equals  $X_R^{3/2}$  with  $X_R$  the ratio of prototype to model dimensions. This study was conducted in weak hydraulic jumps for an inflow Froude number  $Fr_1 = 1.95$  and  $2.1$  across a broad range of inflow conditions and Reynolds numbers. The ratio of conjugate depths  $d_2/d_1$  was not affected by the size of experiment and Reynolds number. Similarly, the experimental observations showed some longitudinal profile of the roller surface, which were very similar for all Reynolds numbers and close to the sidewall photographs (Fig. 2). Altogether, the free-surface profiles of the jump roller were similar for all Reynolds numbers. On another hand, both the

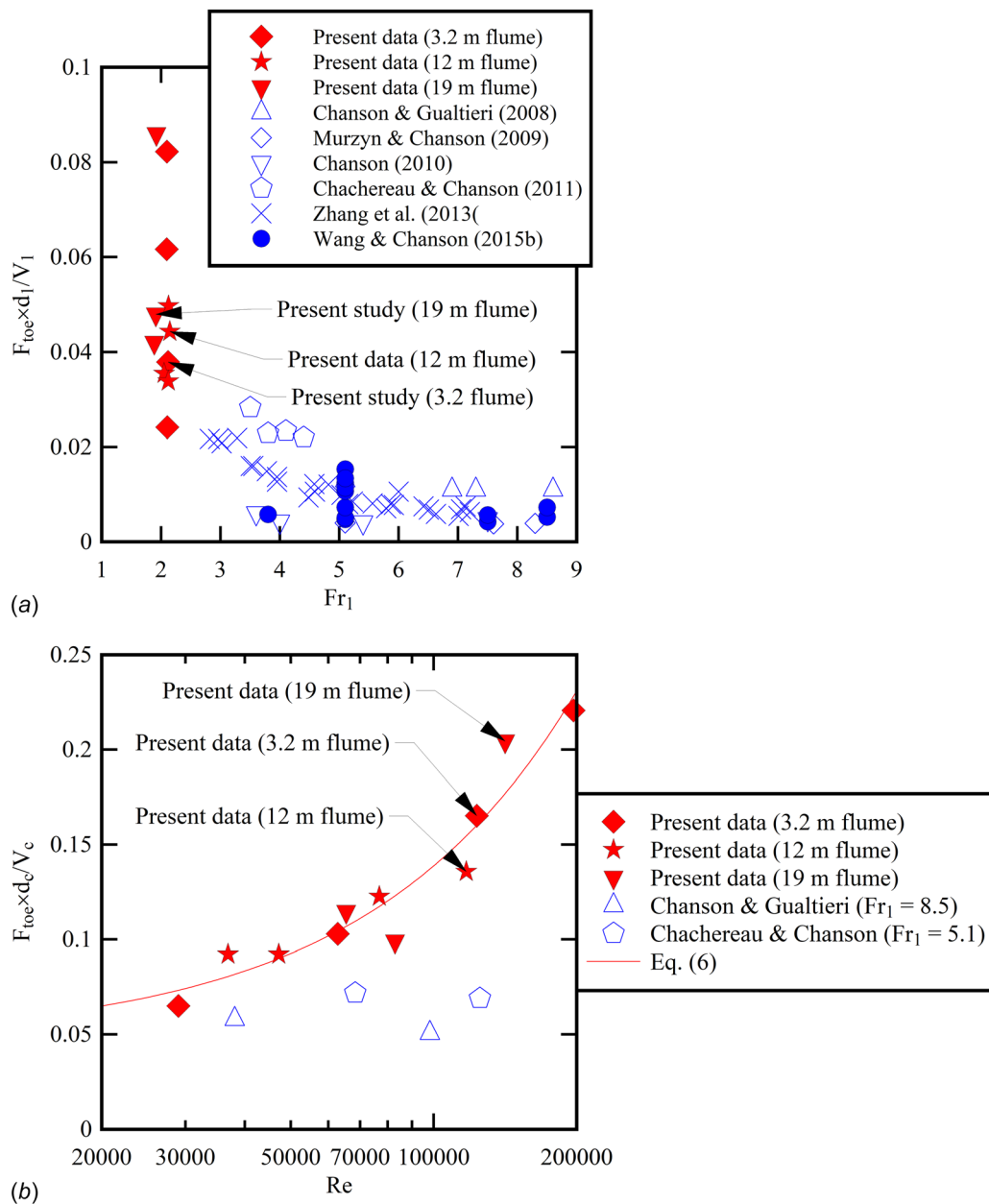


**Fig. 6 Dimensionless fluctuation frequency of longitudinal jump toe positions at low Froude number  $Fr_1 = 1.95$  and  $2.1$  in smooth horizontal rectangular channels—comparison with experimental data in stationary hydraulic jumps [12,27,34,36,38,39]: (a) Strouhal number  $F_{toe} \times d_1 / V_1$  as a function of inflow Froude number  $Fr_1$  and (b) Strouhal number  $F_{toe} \times d_c / V_c$  as a function of Reynolds number  $Re$ —comparison with Eq. (6)**

dimensionless roller length  $L_r/d_1$  and air–water flow region length  $L_{air}/d_1$  showed an increasing trend with increasing Reynolds number in all three experimental channels (Figs. 4 and 5). The roller length data trend was consistent with two earlier data sets [11,34] (Fig. 4). Similarly, the results for the bubbly flow region length were coherent with past photographic observations (Fig. 5). Altogether, the data suggested that the laboratory experiments underestimated both roller length and air–water flow region, and that some full-scale testing is required to prevent scale effects. The dimensionless frequency of the roller toe position fluctuations  $F_{toe} \times d_c / V_c$  about its mean position increased with increasing Reynolds number for  $Fr_1 = 1.95$  and  $2.1$ , without an asymptotic limit (Fig. 6(b)). The finding differed from observations at higher Froude numbers of  $Fr_1 = 5.1$  and  $8.5$ , for which no obvious scale effect was seen to date.

In terms of air concentrations and air entrainment flux, the comparative air–water flow measurements provided some clear guidance on similarity and scale effects. The void fraction data presented the same distribution shapes for  $d_1 > 0.045$  m ( $Re > 6.3 \times 10^4$ ) (Fig. 7). But the depth-averaged air concentration in the roller  $C_{mean}$  was underestimated at the smallest scales, i.e.,  $d_1 < 0.045$  m ( $Re < 6.3 \times 10^4$ ), and similarity was only achieved for  $Re > 1.2 \times 10^5$  (Fig. 8). In comparison, for  $Fr_1 = 5.1$  to  $8.5$ , some self-similarity of the void fraction profiles was observed for  $Re > 2.5 \times 10^4$  [38] and self-similarity of the air entrainment flux for  $Fr_1 = 3.8$  and  $Re > 3.5 \times 10^4$  [48]. The finding suggested a strong interplay between both Froude and Reynolds numbers in the achievement of self-similarity, pointing out the importance of model size in the assessment of air–water properties.

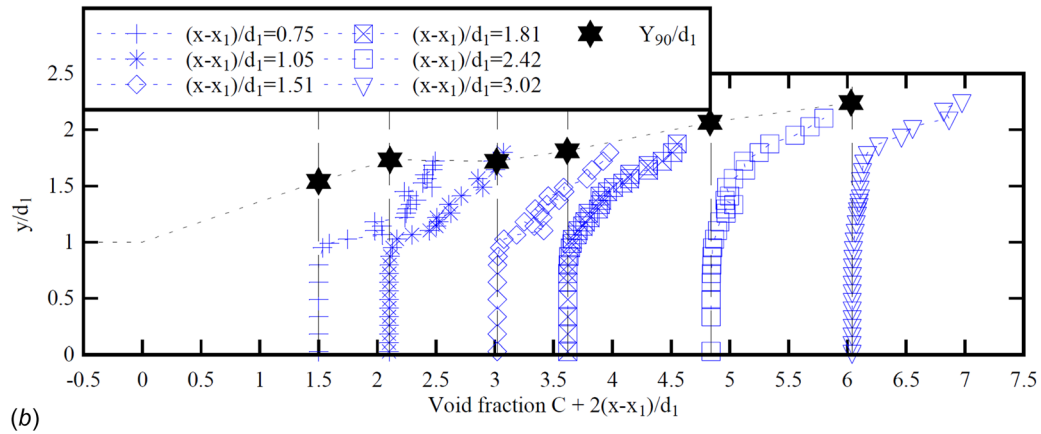
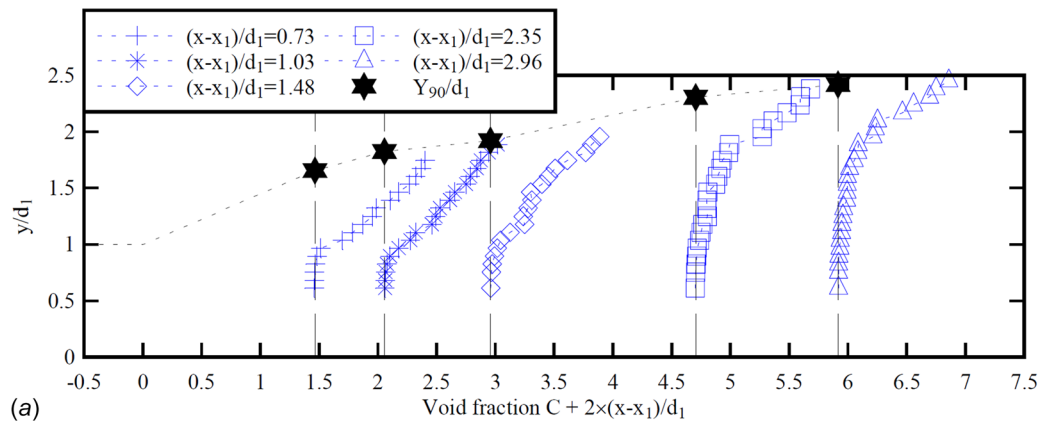


**Fig. 7 Dimensionless distributions of air concentration in the roller of weak hydraulic jump  $Fr_1 = 2.1$  in a smooth horizontal rectangular channel—comparison with the characteristic elevation  $Y_{90}/d_1$ : (a)  $d_1 = 0.071$  m,  $Re = 1.2 \times 10^5$  and (b)  $d_1 = 0.130$  m,  $Re = 3.05 \times 10^5$**

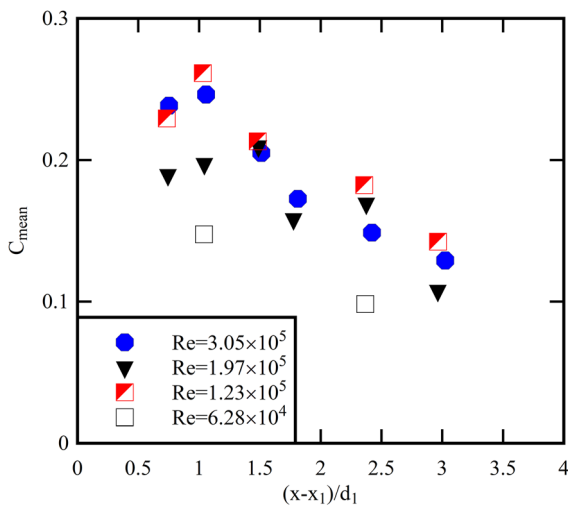


**Fig. 8 Dimensionless longitudinal distributions of depth-averaged air concentration  $C_{mean}$  for weak hydraulic jump  $Fr_1 = 2.1$  in a smooth horizontal rectangular channel**

## 8 Conclusion

A hydraulic jump is a turbulent physical process that remains incompletely understood, especially at large scales relevant in low-head hydraulic structures and geophysical processes. Herein, the hydraulic properties of weak hydraulic jumps were investigated physically in jumps with a Froude number  $Fr_1 = 1.95$  and

$2.1$  and several inflow length scales  $0.012 < d_1 < 0.130$  m. Results showed that, while small inflow depths resulted in a lack of self-aeration, larger values were associated with a fully breaking process with the appearance of strong free-surface turbulence. Overall, the recirculation regions associated with the low Froude number jumps were small, but the free-surface characteristics and the air concentration profiles revealed a certain agreement with hydraulic jumps at higher Froude numbers.

Tests conducted across different scales pointed out the importance of the experiment size, and therefore of the Reynolds number, in physical modeling. While the ratio of conjugate depths  $d_2/d_1$  was not affected by the size of experiment, the dimensionless roller length and length of air–water flow region both showed a marked dependence of the inflow depth and Reynolds number, with increasing dimensionless lengths with increasing inflow length scales. Similarly, the dimensionless frequency of roller toe position fluctuations presented an increasing trend with increasing Reynolds number. The air concentration profiles and air entrainment flux presented qualitatively some similarity for  $d_1 > 0.045$  m ( $Re > 6.3 \times 10^4$ ), but the mean air content, hence the rate of air entrainment, was grossly underestimated for  $d_1 < 0.070$  m ( $Re < 1.2 \times 10^5$ ).

In addition to providing a physical insight on weak hydraulic jumps with  $Fr_1 = 2.1$ , the present physical study also indicated some noticeable scale effects in terms of dimensionless roller length, length of air–water flow region, roller toe fluctuation frequency, and air entrainment, with increasing dimensionless values with increasing Reynolds number. These findings have profound implications for civil, environmental, mechanical and sanitary engineering designs, commonly operating with Reynolds numbers in excess of  $10^5$ , with larger structures operating with  $Re$  well over  $10^6$ .

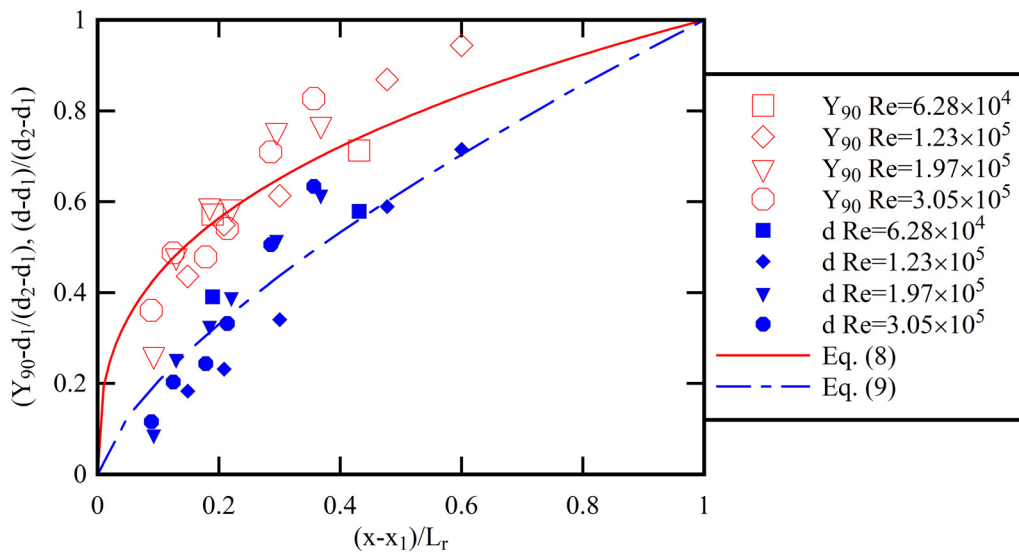


Fig. 9 Self-similarity of free-surface profiles of the roller for  $Fr_1 = 2.1$ : characteristic air–water elevation  $Y_{90}$  and equivalent clear–water depth  $d$ —comparison with Eqs. (8) and (9)

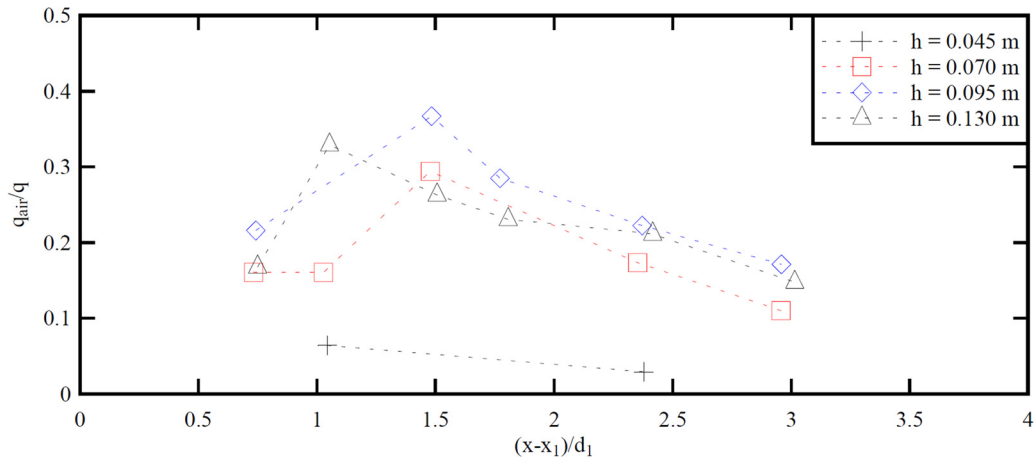


Fig. 10 Longitudinal distributions of the air entrainment flux in hydraulic jumps with low Froude numbers ( $Fr_1 = 2.1$ ) and different Reynolds numbers

## Acknowledgment

The authors thank Professor Michael Pfister (University of Applied Sciences and Arts Western Switzerland, Fribourg), and Professor Carlo Gualtieri (University of Napoli Federico II, Italy), for helpful suggestions. They thank Mr. Rui Shi (The University of Queensland) for technical inputs. The authors acknowledge the technical assistance of Jason Van Der Gevel and Stewart Matthews (The University of Queensland). The financial support of the Swiss National Science Foundation (Grant P2ELP2\_181794) and of the University of Queensland, School of Civil Engineering is acknowledged.

## Data Availability Statement

Some or all data, models, or code that support the findings of this study are available from the corresponding author upon reasonable request. These include the tabular data corresponding to the data presented in Figs. 3–6. Further information is reported in Estrella et al. [50].

## Nomenclature

$B$  = channel breadth  
 $C$  = time-averaged void fraction

$C_{\text{mean}}$  = depth averaged void fraction defined as:

$$C_{\text{mean}} = \frac{1}{Y_{90}} \times \int_{y=0}^{Y_{90}} C \times dy$$

$d$  = equivalent clear-water depth defined as:

$$d = \int_{y=0}^{Y_{90}} (1 - C) \times dy$$

$d_c$  = critical flow depth defined as:  $d_c = (q^2/g)^{1/3}$

$d_1$  = upstream water depth

$d_2$  = downstream water depth

$F_{\text{toe}}$  = main oscillation frequency of the roller toe about its mean position

$Fr_1$  = upstream Froude number:  $Fr_1 = V_1/(g \times d_1)^{1/2}$

$Fr_2$  = downstream Froude number:  $Fr_2 = V_2/(g \times d_2)^{1/2}$

$g$  = gravity acceleration

$h$  = upstream gate opening

$L_{\text{air}}$  = time-averaged length of the bubbly flow region

$L_r$  = roller length, defined as the longitudinal distance between the roller toe position and the location where the water surface became quasi-horizontal

$q$  = unit discharge:  $q = Q/B$

$q$  = unit discharge of entrained air

$Q$  = volume water discharge

$Re$  = Reynolds number:  $Re = \rho \times V_1 \times d_1/\mu$

$S_o$  = longitudinal bed slope

$V_c$  = critical flow velocity defined as:  $V_c = (g \times q)^{1/3}$

$V_x$  = longitudinal velocity component  
 $V_1$  = upstream depth-averaged velocity  
 $V_2$  = downstream depth-averaged velocity  
 $x$  = longitudinal coordinate measured from the upstream end of the flume and positive downstream  
 $x_1$  = longitudinal location of roller toe  
 $X_R$  = geometric scaling ratio of prototype to model dimensions  
 $y$  = vertical elevation above the channel bed  
 $Y_{90}$  = characteristic elevation above the bed where the void fraction is  $C = 0.90$   
 $\mu$  = dynamic viscosity of water  
 $\rho$  = water density  
 $\varnothing$  = diameter

## Subscripts

$c$  = critical flow conditions  
 $1$  = upstream flow conditions  
 $2$  = downstream flow conditions

## References

- [1] Bakhmeteff, B. A., and Matzke, A. E., 1936, "The Hydraulic Jump in Terms of Dynamic Similarity," *Trans., ASCE*, **101**(1), pp. 630–647.
- [2] Bidone, G., 1819, "Le Remou et Sur la Propagation Des Ondes. ('The Jump and on the Wave Propagation.')." Report to Académie Royale des Sciences de Turin, séance 12 Dec., Vol. XXV, pp. 21–112 (in French).
- [3] Hager, W. H., 1992, *Energy Dissipators and Hydraulic Jump*, Vol. 8, Kluwer Academic Publ., Water Science and Technology Library, Dordrecht, The Netherlands, p. 288..
- [4] Ryabenko, A. A., 1990, "Conditions Favorable to the Existence of an Undulating Jump," *Gidrotekh. Stroit.*, **24**(12), pp. 762–34(in Russian).
- [5] Bakhmeteff, B. A., 1932, *Hydraulics of Open Channels*, 1st ed., McGraw-Hill, New York, p. 329.
- [6] Henderson, F. M., 1966, *Open Channel Flow*, MacMillan Company, New York.
- [7] Chow, V. T., 1973, *Open Channel Hydraulics*, McGraw-Hill International, New York.
- [8] Bélanger, J. B., 1841, "Notes Sur L'Hydraulique. ('Notes on Hydraulic Engineering.')." Ecole Royale Des Ponts et Chaussées, Paris, France, p. 223 pages (in French).
- [9] Lennon, J. M., and Hill, D. F., 2006, "Particle Image Velocimetry Measurements of Undular and Hydraulic Jumps," *J. Hydraul. Eng., ASCE*, **132**(12), pp. 1283–1294.
- [10] Misra, S. K., Thomas, M., Kambhmettu, C., Kirby, J. T., Veron, F., and Brocchini, M., 2006, "Estimation of Complex Air–Water Interfaces From Particle Image Velocimetry Images," *Exp. Fluids*, **40**(5), pp. 764–775.
- [11] Murzyn, F., Mouaze, D., and Chaplin, J. R., 2007, "Air–Water Interface Dynamic and Free Surface Features in Hydraulic Jumps," *J. Hydraulic Res., IAHR*, **45**(5), pp. 679–685.
- [12] Chachereau, Y., and Chanson, H., 2011, "Bubbly Flow Measurements in Hydraulic Jumps With Small Inflow Froude Numbers," *Int. J. Multiphase Flow*, **37**(6), pp. 555–564.
- [13] Mignot, E., and Cienfuegos, R., 2011, "Spatial Evolution of Turbulence Characteristics in Weak Hydraulic Jumps," *J. Hydraul. Res., IAHR*, **49**(2), pp. 222–230.
- [14] Lin, C., Hsieh, S. C., Lin, I. J., Chang, K. A., and Raikar, R. V., 2012, "Flow Property and Self-Similarity in Steady Hydraulic Jumps," *Exp. Fluids*, **53**(5), pp. 1591–1616.
- [15] Montano, L., and Felder, S., 2020, "An Experimental Study of Air–Water Flows in Hydraulic Jumps on Flat Slopes," *J. Hydraul. Res., IAHR*, **58**(5), pp. 767–777.
- [16] Novak, P., and Cabelka, J., 1981, "Models in Hydraulic Engineering," *Physical Principles and Design Applications*, Pitman Publication, London, p. 459.
- [17] British Standard, 1943, *Flow Measurement*, British Standard Institution, London, Standard No. Code BS 1042:1943.
- [18] Neal, L. S., and Bankoff, S. G., 1963, "A High Resolution Resistivity Probe for Determination of Local Void Properties in Gas–Liquid Flows," *Am. Inst. Chem. JI*, **9**, pp. 49–54.
- [19] Jones, O. C., and Delhaye, J. M., 1976, "Transient and Statistical Measurement Techniques for two-Phase Flows: A Critical Review," *Int. J. Multiphase Flow*, **3**(2), pp. 89–116.
- [20] Chanson, H., 2002, "Air–Water Flow Measurements With Intrusive Phase-Detection Probes. Can we Improve Their Interpretation?," *J. Hydraul. Eng., ASCE*, **128**(3), pp. 252–255.
- [21] Brocchini, M., and Peregrine, D. H., 2001, "The Dynamics of Strong Turbulence at Free Surfaces. Part 1. Description," *J. Fluid Mech.*, **449**, pp. 225–254.
- [22] Goodwin, R. P., 1993, "The Hydraulic Jump (Shocks and Viscous Flow in the Kitchen Sink)," *Am. J. Phys.*, **61**(9), pp. 829–832.
- [23] Aristoff, J. M., Leblanc, J. D., Hosoi, A. E., and Bush, J. W. M., 2004, "Viscous Hydraulic Jumps," *Phys. Fluids*, **16**(9), pp. S4–S4.
- [24] Ervine, D. A., and Falvey, H. T., 1987, "Behaviour of Turbulent Water Jets in the Atmosphere and in Plunge Pools," *Proc. Inst. Civ. Eng., London*, **83**(1), pp. 295–314.
- [25] Montano, L., Li, R., and Felder, S., 2018, "Continuous Measurements of Time-Varying Free-Surface Profiles in Aerated Hydraulic Jumps With a LIDAR," *Exp. Therm. Fluid Sci.*, **93**, pp. 379–397.
- [26] Mouaze, D., Murzyn, F., and Chaplin, J. R., 2005, "Free Surface Length Scale Estimation in Hydraulic Jumps," *ASME J. Fluids Eng.*, **127**(6), pp. 1191–1193.
- [27] Murzyn, F., and Chanson, H., 2009, "Free-Surface Fluctuations in Hydraulic Jumps: Experimental Observations," *Exp. Therm. Fluid Sci.*, **33**(7), pp. 1055–1064.
- [28] Kalinske, A. A., and Robertson, J. M., 1943, "Closed Conduit Flow," *Trans., ASCE*, **108**(1), pp. 1435–1447.
- [29] Lubin, P., Kimmoun, O., Veron, F., and Glockner, S., 2019, "Discussion on Instabilities in Breaking Waves: Vortices, Air-Entrainment and Droplet Generation," *Eur. J. Mech./B Fluids*, **73**, pp. 144–156.
- [30] Schröder, R., 1963, "Die Turbulente Strömung im Freien Wechselsprung," *Mitteilungen*, Institut Für Wasserbau Und Wasserwirtschaft, Tech. Univ. Berlin, Germany, No. 59 (in German).
- [31] Wang, H., and Chanson, H., 2015, "Air Entrainment and Turbulent Fluctuations in Hydraulic Jumps," *Urban Water J.*, **12**(6), pp. 502–518.
- [32] Chanson, H., 2009, "Development of the Bélanger Equation and Backwater Equation by Jean-Baptiste Bélanger (1828)," *J. Hydraul. Eng., ASCE*, **135**(3), pp. 159–163.
- [33] Hager, W. H., Bremen, R., and Kawagoshi, N., 1990, "Classical Hydraulic Jump: Length of Roller," *J. Hydraul. Res., IAHR*, **28**(5), pp. 591–608.
- [34] Wang, H., and Chanson, H., 2015b, "Experimental Study of Turbulent Fluctuations in Hydraulic Jumps," *J. Hydraul. Eng., ASCE*, **141**(7), p. 04015010.
- [35] Leng, X., and Chanson, H., 2015, "Turbulent Advances of a Breaking Bore: Preliminary Physical Experiments," *Exp. Therm. Fluid Sci.*, **62**, pp. 70–77.
- [36] Chanson, H., 2010, "Convective Transport of Air Bubbles in Strong Hydraulic Jumps," *Int. J. Multiphase Flow*, **36**(10), pp. 798–814.
- [37] Long, D., Rajaratnam, N., Steffler, P. M., and Smy, P. R., 1991, "Structure of Flow in Hydraulic Jumps," *J. Hydraul. Res., IAHR*, **29**(2), pp. 207–218.
- [38] Chanson, H., and Gualtieri, C., 2008, "Similitude and Scale Effects of Air Entrainment in Hydraulic Jumps," *J. Hydraul. Res., IAHR*, **46**(1), pp. 35–44.
- [39] Zhang, G., Wang, H., and Chanson, H., 2013, "Turbulence and Aeration in Hydraulic Jumps: Free-Surface Fluctuation and Integral Turbulent Scale Measurements," *Environ. Fluid Mech.*, **13**(2), pp. 189–204.
- [40] Simoni, D., Ubaldi, M., and Zunino, P., 2016, "A Simplified Model Predicting the Kelvin–Helmholtz Instability Frequency for Laminar Separated Flows," *ASME J. Turbomach.*, **138**(4), p. 6.
- [41] Yang, Z., and Voke, P. R., 2001, "Large-Eddy Simulation of Boundary-Layer Separation and Transition at a Change of Surface Curvature," *J. Fluid Mech.*, **439**, pp. 305–333.
- [42] Rajaratnam, N., 1962, "An Experimental Study of Air Entrainment Characteristics of the Hydraulic Jump," *J. Inst. Eng. India*, **42**(7), pp. 247–273.
- [43] Chanson, H., and Brattberg, T., 2000, "Experimental Study of the Air–Water Shear Flow in a Hydraulic Jump," *Int. J. Multiphase Flow*, **26**(4), pp. 583–607.
- [44] Murzyn, F., Mouaze, D., and Chaplin, J. R., 2005, "Optical Fibre Probe Measurements of Bubbly Flow in Hydraulic Jumps," *Int. J. Multiphase Flow*, **31**(1), pp. 141–154.
- [45] Mossa, M., and Tolve, U., 1998, "Flow Visualization in Bubbly Two-Phase Hydraulic Jump," *ASME J. Fluids Eng.*, **120**(1), pp. 160–165.
- [46] Wang, H., 2014, "Turbulence and Air Entrainment in Hydraulic Jumps," Ph.D. thesis, School of Civil Engineering, The University of Queensland, Brisbane, Australia, p. 341.
- [47] Valiani, A., 1997, "Linear and Angular Momentum Conservation in Hydraulic Jump," *J. Hydraul. Res., IAHR*, **35**(3), pp. 323–354.
- [48] Wang, H., and Chanson, H., 2018, "Estimate of Void Fraction and Air Entrainment Flux in Hydraulic Jump Using Froude Number," *Can. J. Civ. Eng.*, **45**(2), pp. 105–116.
- [49] Rouse, H., 1938, *Fluid Mechanics for Hydraulic Engineers*, McGraw-Hill, New York.
- [50] Estrella, J., Wüthrich, D., and Chanson, H., 2021, "Two-phase Air–water Flow Properties in Hydraulic Jump at Low Froude Number: Scale Effects in Physical Modelling. Hydraulic Model." The University of Queensland, Brisbane, Australia, p. 157, Report No. CH120/21.